Fjords in viscous fingering: Selection of width and opening angle

Leif Ristroph,[1] Matthew Thrasher,[1,*] Mark B. Mineev-Weinstein,[2] and Harry L. Swinney[1]

[1]*Center for Nonlinear Dynamics and Department of Physics, University of Texas at Austin, Austin, Texas 78712, USA*

[2]*Applied Physics Division, MS-P365, Los Alamos National Laboratory, Los Alamos, New Mexico 87545, USA*

Our experiments on viscous fingering of air into oil contained between closely spaced plates reveal two selection rules for the fjords of oil that separate fingers of air. (Fjords are the building blocks of solutions of the zero-surface-tension Laplacian growth equation.) Experiments in rectangular and circular geometries yield fjords with base widths $\lambda_c/2$, where λ_c is the most unstable wavelength from a linear stability analysis. Further, fjords open at an angle of $8.0° \pm 1.0°$. These selection rules hold for a wide range of pumping rates and fjord lengths, widths, and directions.

Similar growth patterns have been found for viscous fingering, bacterial growth, flame propagation, dielectric breakdown, electrodeposition, solidification, metal corrosion, and diffusion-limited aggregation (DLA) [1]. Analysis of these interfacial patterns is daunting because of the broad range of length scales, as illustrated by our experiments on fingering of air in thin oil layers (Fig. 1). The interface becomes increasingly ramified with increasing forcing strength, which is characterized by the capillary number

$$Ca = \frac{\mu V}{\sigma}, \qquad (1)$$

where μ is the viscosity of the oil, V is the local interfacial velocity, and σ is the surface tension of the air-oil interface.

Most theoretical work on viscous fingering has concentrated on fingers rather than fjords, but fjords have been considered as building blocks of a theory of Laplacian growth in an analysis of a two-dimensional inviscid fluid penetrating a viscous fluid (with zero interfacial tension) [2]. The exact solutions for the interface are free of finite-time singularities and are linear combinations of logarithmic terms, each term representing a single straight fjord with parallel walls. While these analytic solutions have helped in the understanding of the growth of complex growth patterns, experiments indicate fjords can have curved trajectories and nearly always have a nonzero opening angle (Fig. 1) [3].

Most experiments have also concentrated on fingers, but a few experiments have examined fjords [3]. For the circular sector ("wedge") geometry, Thomé *et al.* measured the angular gap between a wall and a divergent finger (at a point 12 cm from the vertex) to be approximately 5° for divergent sector angles between 20° and 50° [4]. Their sector decomposition method considered finger growth in terms of wedges whose "virtual walls" were fjord centerlines; this approach suggests that a fjord opening angle should be about 10°, i.e., twice the angle measured by Thomé *et al.* [4]. Theoretical analyses [5,6] yielded an estimate corresponding to a fjord opening angle of 11.7° [6]. Other work has suggested that the

width of a fjord relative to the width of the splitting finger has values between $\frac{1}{8}$ and $\frac{1}{3}$ [3,4,7,8].

Despite much effort, selection laws are lacking for ramified fingers in either rectangular [Figs. 1(a) and 1(b)] or circular geometries [Figs. 1(c) and 1(d)]. We find that fjords in both geometries have a well-defined base width that is determined by the characteristics of the interface at the fjord's birth (when a finger splits). Further, we find that fjords open at an angle that is close to 8°. The selection rules for the fjord width and opening angle hold for a wide variation in the ramification of the patterns.

Experimental apparatus. — Interfacial patterns were grown in both rectangular and circular Hele-Shaw cells (closely spaced glass plates) filled with oil. Air was forced into the oil, creating an unstable interface (Fig. 1). In the rectangular geometry, two pieces of glass (each 1.91 cm thick), separated by a gap of 0.0508 cm, bounded a cell 25.4 cm wide by 254 cm long [9]. The maximum variation in gap thickness at the center of the cell (due to the imposed
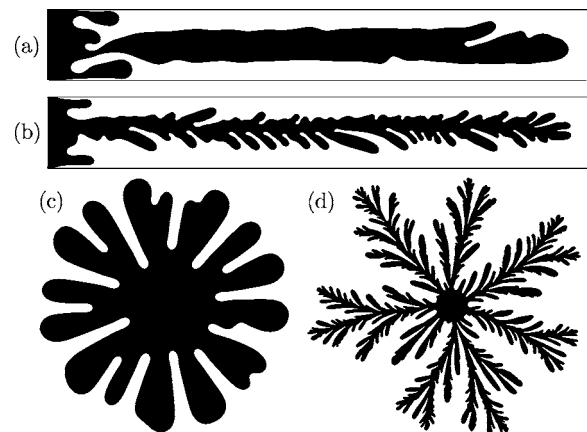

FIG. 1. Viscous fingering patterns of air (black) penetrating into oil (white) in rectangular and circular Hele-Shaw cells for different forcing levels. A fjord is the region of oil between two adjacent fingers. Rectangular cell: Ca=(a) 0.0056 and (b) 0.046; the rectangles are 25 cm wide and 190 cm long, while the entire cell is 254 cm long. Circular cell: Ca=(c) 0.000 88 and (d) 0.27; the radial patterns are approximately 20 cm in diameter, grown in a cell of diameter 28.8 cm. The Ca values were computed using the average velocity of the farthest tip.
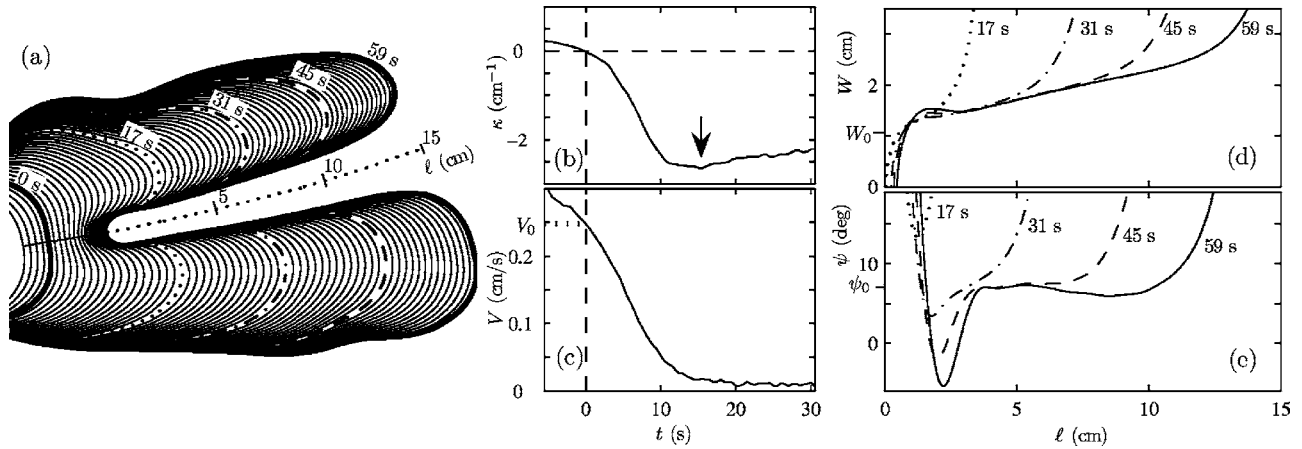
---

*Electronic address: thrasher@chaos.utexas.edu

FIG. 2. (a) Time development of a fjord grown in the rectangular cell at Ca=0.0076 (cf. Fig. 1 caption). Adjacent interfaces are separated by 1 s. (b) Curvature κ and (c) velocity V of the point on the finger ($\kappa > 0$) that evolves into a fjord ($\kappa < 0$) and stops moving; $t=0$ is the time at which $\kappa=0$. The velocity V_0 used in computing the instability wavelength λ_c [Eq. (2)] corresponds to $\kappa=0$; here $V_0 = 0.25 \pm 0.01$ cm/s. The arrow points to the minimum of curvature in time, which defines the fjord centerline arc length $\ell=0$. (d) Fjord width W as a function of the fjord centerline arc length ℓ. The base width of the fjord, W_0, is given by the fjord width extrapolated to $\ell=0$; here $W_0 = 1.08 \pm 0.06$ cm. (e) The selected opening angle of the fjord, given by the plateau in $\psi(\ell)$, is $\psi_0 = 7.1° \pm 0.5°$.

pressure gradient) was less than 3%, even at the highest pump rate [9]. The cell was filled with silicone oil (viscosity $\mu = 50.6$ mPa s and surface tension $\sigma = 20.5$ mN/m at 24 °C); the oil wets the glass completely. A uniform flow rate was achieved using a syringe pump to withdraw oil from a reservoir at one end of the channel; an air reservoir at atmospheric pressure was attached to the other end. The channel was illuminated from below. Each full interface, as in Figs. 1(a) and 1(b), was constructed from 11 images (each 1300×1030 pixels, 0.21 mm/pixel), which were obtained using a camera and rotating mirror. Alternatively, the camera was focused on a fixed 22-cm-long section of the channel to obtain a time resolution of 12 frames/s [Fig. 2(a)].

In the radial geometry, air was forced into an oil-filled gap through a hole in the center of the bottom glass plate. Each optically polished glass plate had a diameter of 28.8 cm and a thickness of 6.0 cm. The two plates were separated by a gap thickness of 0.0127 cm (uniform to 1%) [10,11]. The gap and an annular reservoir were filled with silicone oil (viscosity $\mu = 345$ mPa s and surface tension $\sigma = 20.9$ mN/m at 24 °C). Interfacial patterns were grown either by maintaining a constant pressure difference between the oil reservoir and air or by using a syringe pump to remove oil from the buffer. Images of resolution 0.32 mm/pixel were acquired at up to 12 frames/s.

Fjord characteristics. — From the images we determined, as a function of time, the interface's velocity V and curvature κ, the fjord width W, and the fjord opening angle ψ (Fig. 2). The most unstable (critical) wavelength of a curved interface between a less viscous fluid forced into a more viscous fluid is given by [12,13]

$$\lambda_c = \frac{\pi}{\sqrt{\text{Ca}/b^2 + \kappa^2/12}} \approx \frac{\pi b}{\sqrt{\text{Ca}}} = \pi b \sqrt{\frac{\sigma}{\mu V}}, \qquad (2)$$

where b is the cell gap thickness and κ is the interface curvature (not including the curvature in the small gap dimen-

sion) at the point where the finger becomes unstable [14–17]. For all interfaces that we examined, the curvature term in Eq. (2) was about two orders of magnitude smaller than the term involving the capillary number Ca; hence we made the flat interface ($\kappa=0$) approximation in computing λ_c.

When a finger became unstable, the finger flattened and a fjord was born. A normal projection algorithm was used to track the fjord trajectory back in time to earlier interfaces [solid, nearly straight line on the left in Fig. 2(a)]. (The fjord location for an earlier interface was identified by projecting a ray normally from the later interface until it intersected the earlier one.) The time evolution of the local curvature κ then revealed the birth of the fjord, where $\kappa=0$ [Fig. 2(b)]. The velocity V_0 at this point [Fig. 2(c)] was used in Eq. (2) to calculate λ_c. The uncertainty in λ_c is 9%; film wetting corrections [14,15] and the velocity measurements are the main sources of uncertainty.

Once a fjord developed, we determined its width W as a function of the arc length ℓ of its centerline, as illustrated in Fig. 2(d). The fjord centerline was found by beginning with a point on the side of the fjord; then the closest point on the opposite side was found such that the interior angles between the two local tangents and the line connecting the two points were the same. The midpoint of the connecting line gave a point on the fjord centerline. Repeating this procedure for each point on the side of the fjord constructed the centerline. The fjord base point ($\ell=0$) was taken to correspond to the minimum of curvature along the fjord's trajectory [Fig. 2(b)]. As surface tension relaxed the interface, a fjord's base moved forward. The distance a base moved after $t=0$ was corrected by adding the same distance to the arc length [Fig. 2(d)].

Curves $W(\ell)$ obtained for different fjords exhibited the same structure: $W(\ell)$ initially grew quickly with increasing ℓ due to the rounded nature of the fjord base, but soon $W(\ell)$ increased linearly with ℓ. The fjord base width W_0 was measured as follows: for each ℓ the local tangent of $W(\ell)$ was linearly extrapolated back to $\ell=0$, a histogram of extrapo-
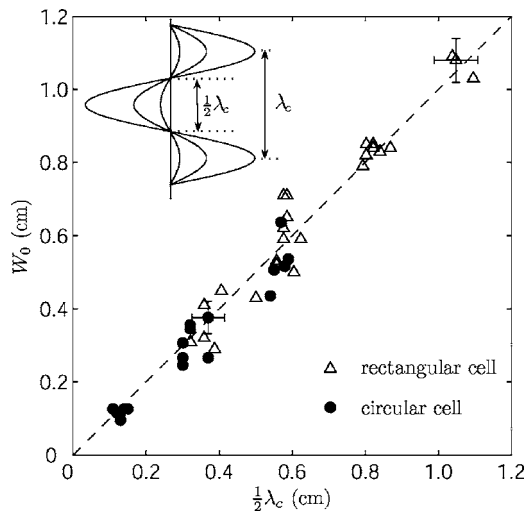
FIG. 3. The measured fjord base width W_0 [Fig. 2(d)] versus the predicted width $\lambda_c/2$, where λ_c is the instability wavelength, Eq. (2). The inset illustrates how an initial infinitesimal perturbation of a front sets the wavelength for a large-amplitude fjord. Here, the front is moving to the right and is observed in a comoving frame. The lengths of the error bars are the rms deviations from the line.

lated base widths was made, and the histogram's peak gave W_0. For an individual fjord measured over a wide range of times, this procedure yielded a fjord base width with a typical uncertainty of 6%. Confinement by neighboring fjords caused a slightly increasing extrapolated fjord base width with increasing values of ℓ.

The observed linear increase in $W(\ell)$ suggested an almost constant opening angle: $\psi = \arctan\left(\frac{dW}{d\ell}\right)$. The angle $\psi(\ell)$ had the same qualitative evolution for all fjords: a fjord began with an opening angle of 180°, followed by a surface-tension-induced dip, followed by a peak and a plateau (usually with a slightly negative slope), and finally a rapid increase at the fjord's end [Fig. 2(e)]. We defined the opening angle ψ_0 to be the peak of the histogram of ψ values generated from plots of $\psi(\ell)$. The angle selected was always about 8°; the uncertainty in the opening angle for a single fjord was 0.5°.

Fjord base width. — We predict that the base width of a fjord is determined at the onset of the instability of the moving interface, as illustrated by the inset of Fig. 3. The critical wavelength λ_c given by a linear stability analysis of the infinitesimally perturbed flat front, Eq. (2), determines the distance between adjacent fingers when they are born, and the base width of the macroscopic fjord that develops between the two emergent fingers is $W_0 = \frac{1}{2}\lambda_c$. A comparison between measurements and the predicted widths requires a value for the velocity V in the expression for the capillary number Ca. Lajeunesse and Couder suggest that a perturbation on a finger is the "precursor" of tip splitting and confirm that the perturbation's wavelength is "of the order of 1.5 λ_c [3]." Our approach tests this idea at the instability's onset, making the assumption that $V = V_0$ is measured at the point on the fjord's trajectory corresponding to $\kappa = 0$ [Figs. 2(b) and 2(c)].

Measurements of the fjord base widths W_0 in both the circular and rectangular geometries agree well with the
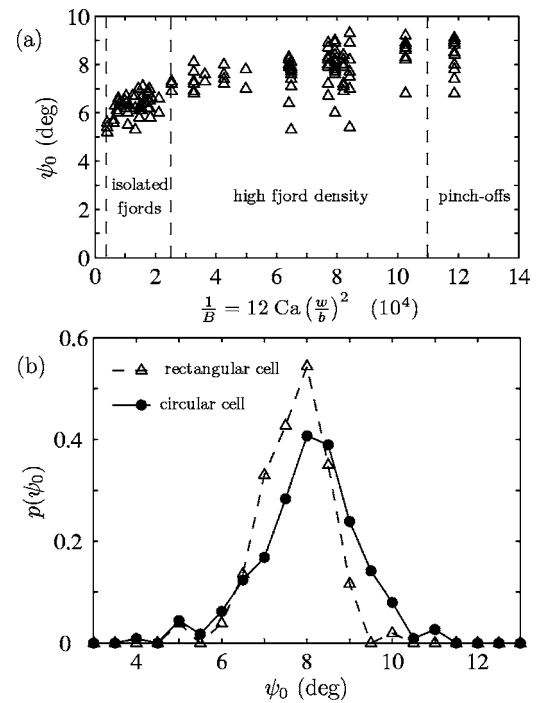

FIG. 4. (a) The fjord opening angle ψ_0 in the rectangular cell increases slightly with forcing parameter (the modified capillary number $1/B$). (b) Probability distributions $p(\psi_0)$ measured for the opening angle of all fjords observed in the circular cell (●) and of fjords in the high-fjord-density regime ($1/B > 25\,000$) of the rectangular cell (△). The data for the rectangular and circular cells yield, respectively, $\psi_0 = 7.9° \pm 0.8°$ and $\psi_0 = 8.2° \pm 1.1°$, where the uncertainties are one standard deviation.

predicted widths, as Fig. 3 illustrates. The fjord widths varied by an order of magnitude as the control conditions were varied widely (pump rates were 0.17–2.00 cm^3/s in the rectangular cell and $0.000\,83$–0.033 cm^3/s in the circular cell, and in the latter geometry, measurements were also made for pressure differences of 0.10 and 0.25 atm). The local forcing strength at the birth of a fjord is affected by nearby fjords, walls, and details of the interface, so a given global pumping rate can yield fjords with different properties. The uncertainties in λ_c and W_0 are 9% and 6%, respectively. The observed scatter in Fig. 3 is consistent with these estimated errors.

Fjord opening angle. — The opening angle ψ_0 measured in the rectangular geometry is shown in Fig. 4(a) as a function of the appropriate forcing parameter for this geometry, the modified capillary number $1/B = 12\mathrm{Ca}(w/b)^2$ (where w is the channel width) [9,18], which was computed using the average velocity of the farthest finger tip. Isolated fjords occur in the regime just beyond the onset of tip splitting, which occurs for $1/B \approx 4000$ [18,19].

For $1/B > 25\,000$, the pattern develops a high density of fjords. Despite the wide range of experimental parameters in this regime, the measured angles are surprisingly similar. The results for the distribution of opening angles in the circular cell are indistinguishable from those for ramified patterns in the rectangular cell: the probability distribution function $p(\psi_0)$ has the same form with essentially the same mean 8° and same standard deviation 1° [Fig. 4(b)]. We suggest that

the near constancy of the opening angle is fundamental to scale invariance and fractal dimension. Our result is consistent both with efforts to relate the multifractal dimensions of a fully developed fingering structure [20] with the fjords' opening angle [21] and with a recent observation [11] of an invariant unscreened angle distribution in a fractal grown in a radial geometry. While intriguing, the connection between these invariant geometrical characteristics remains obscure.

Conclusions. — We have presented two selection rules for the geometric form of fjords in rectangular and circular cells. The base width selected by the fjords has been found to be well described by $W_0 = \frac{1}{2}\lambda_c$, where λ_c is the local critical wavelength. This selection rule provides insight into the most apparent difference in viscous fingering patterns: highly forced patterns are composed of thinner fjords. The rule is based on universal features of Laplacian growth and does not invoke any specific properties of viscous fingering in a Hele-Shaw cell. Therefore, we conjecture that this rule should apply not only to viscous fingering, but also to other isotropic Laplacian growth problems.

The second selection rule is obtained from measurements of the opening angle as a function of arc length along the fjord centerline: for a broad range of experimental parameters and for both circular and rectangular geometries, the selected opening angle ψ_0 was always near $8°$; we have no explanation for this result. The two selection rules hold for a wide range of fjord widths, lengths, and degrees of bending, and for a wide range of angles of fjord directions with respect to the rectangular cell axis or with respect to radial lines in the circular cell.

[1] Y. Couder, *Perspectives in Fluid Dynamics*, edited by G. K. Batchelor, H. K. Moffat, and M. G. Worster (Cambridge University Press, Cambridge, U.K., 2000), pp. 53–104.

[2] M. B. Mineev-Weinstein and S. P. Dawson, Phys. Rev. E **50**, R24 (1994).

[3] E. Lajeunesse and Y. Couder, J. Fluid Mech. **419**, 125 (2000).

[4] H. Thomé, M. Rabaud, V. Hakim, and Y. Couder, Phys. Fluids A **1**, 224 (1989).

[5] M. BenAmar, Phys. Rev. A **43**, R5724 (1991).

[6] Y. Tu, Phys. Rev. A **44**, 1203 (1991).

[7] L. Paterson, J. Fluid Mech. **113**, 513 (1981).

[8] A. Pereira and J. Elezgaray, Phys. Rev. E **69**, 026301 (2004).

[9] M. G. Moore, A. Juel, J. M. Burgess, W. D. McCormick, and H. L. Swinney, Phys. Rev. E **65**, 030601(R) (2002).

[10] E. Sharon, M. G. Moore, W. D. McCormick, and H. L. Swinney, Phys. Rev. Lett. **91**, 205504 (2003).

[11] O. Praud and H. L. Swinney, Phys. Rev. E **72**, 011406 (2005).

[12] R. L. Chuoke, P. van Meurs, and C. van der Pol, Trans. AIME **216**, 188 (1959).

[13] J. Bataille, Rev. Inst. Fr. Pet. Ann. Combust. Liq. **23**, 1349 (1968).

[14] C.-W. Park and G. M. Homsy, J. Fluid Mech. **139**, 291 (1984).

[15] L. Schwartz, Phys. Fluids **29**, 3086 (1986).

[16] J.-D. Chen, J. Fluid Mech. **201**, 223 (1989).

[17] In previous work, Chen [16] measured the instability wavelength as a function of Ca. Park and Homsy [14] and Schwartz [15] calculated corrections due to the surface tension and film wetting.

[18] C. W. Park and G. M. Homsy, Phys. Fluids **28**, 1583 (1985).

[19] The isolated fjords have a selected opening angle $\psi_0 = 6.3° \pm 0.4°$, which is lower than the angle measured in fjords grown with $1/B > 25\,000$. These fjords are strongly confined by the walls.

[20] J. Mathieson, I. Procaccia, M. Thrasher, and H. L. Swinney, cond-mat/0512274.

[21] S. K. Sarkar, Phys. Rev. Lett. **65**, 2680 (1990).